Principles of Diffusion Tensor Imaging and Its Applications to Basic Neuroscience Research

Primer

Susumu Mori[1,2,*] and Jiangyang Zhang[1]
[1] Department of Radiology
Division of NMR
Johns Hopkins University
School of Medicine
720 Rutland Avenue
Baltimore, Maryland 21205
[2] F.M. Kirby Research Center for
    Functional Brain Imaging
Kennedy Krieger Institute
707 North Broadway
Baltimore, Maryland 21205

The brain contains more than 100 billion neurons that communicate with each other via axons for the formation of complex neural networks. The structural mapping of such networks during health and disease states is essential for understanding brain function. However, our understanding of brain structural connectivity is surprisingly limited, due in part to the lack of noninvasive methodologies to study axonal anatomy. Diffusion tensor imaging (DTI) is a recently developed MRI technique that can measure macroscopic axonal organization in nervous system tissues. In this article, the principles of DTI methodologies are explained, and several applications introduced, including visualization of axonal tracts in myelin and axonal injuries as well as human brain and mouse embryonic development. The strengths and limitations of DTI and key areas for future research and development are also discussed.

Introduction

The human brain consists of more than 100 billion neurons, and it is arguably the most complex structure in our body. Imaging has been a powerful technique to navigate us through this vast entity and identify the places where biological events of interest occur. In animal studies, histology followed by examination with light or electron microscopy has been one of the most widely used imaging methods. Various staining techniques can highlight the locations of proteins and genes of interests, and electron microscopy can extend our observation to objects at the molecular level. However, histology-based imaging has several serious drawbacks. First, it is invasive. Second, its labor-intensive and destructive nature makes it a nonideal choice for examining the entire brain or for performing quantitative three-dimensional analyses. MRI is probably at the other end of the spectrum of imaging modalities. It is noninvasive, three-dimensional, and requires as little as a few minutes to characterize the entire brain anatomy. The end results are often merely a few megabytes (MBs) of data, in which all the relevant brain information is condensed by a consistent sampling scheme. Its strength is, however, also its weakness. While the brain anatomical information is condensed, much biological informa-

tion is degenerated, which causes a loss of specificity and sensitivity to certain biological processes. It is a never-ending quest for the MRI research community to attempt to recover more types of biological information that would otherwise be lost with conventional MRI techniques. In this review, we would like to introduce a new MRI technique called diffusion tensor imaging (DTI). This imaging technique can delineate the axonal organization of the brain, which we could not appreciate with conventional MRI. DTI was introduced in the mid 1990s (Basser et al., 1994), and its applications to small animal studies have only recently been initiated (Ahrens et al., 1998; Harsan et al., 2006; Kroenke et al., 2006; Mori et al., 2001; Nair et al., 2005). The purpose of this review is to explain how DTI works and to introduce state-of-the-art neuroscience research using DTI.

How DTI Works

Limitations of MRI and the Importance of Contrast Generation

Before introducing DTI, we want to highlight the importance of image contrast in MRI. MRI is based on signals from ^{1}H (proton) nuclei. There are many molecules that contain protons in our body, but we can assume that the signal in DTI studies is dominated by water protons. Unless we are interested in water itself, the MRI signal is an indirect indicator of biological events in the brain. This is always an issue when we interpret MRI results. From an experimental point of view, there are two important limitations in MRI. These are spatial resolution and contrast. The physical limitation of MR image resolution is thought to be about 10 μm. This is because water molecules move about this much during the typical MR measurement time (10–100 ms). It is similar to taking a photo of a fast-moving car, and the MR measurement time is similar to shutter speed. We inevitably lose image sharpness beyond 10 μm. Practically, this resolution is difficult to achieve because water signal from such a small pixel becomes too weak to emerge from noise, and the scanning time becomes too long to detect such a weak signal by a large number of signal averages. In Figure 1A, examples of in vivo and ex vivo mouse brain images are shown. For in vivo studies, we have a short scanning time (typically 0.5–2.0 hr), which limits the resolution we can achieve. This limitation in scanning time is less an issue for ex vivo fixed samples, and we can achieve much higher resolution (Jacobs and Fraser, 1994; Johnson et al., 1993; Smith et al., 1996).

Another practical limitation of resolution is, interestingly, the data size, especially for ex vivo studies. For example, if we achieve 20 μm resolution in a mouse brain, which typically has a dimension of 10–15 mm, a 3D image would have about 500 pixels for each dimension. For an integer matrix, this amounts to $500 \times 500 \times 500 \times 2$ bytes = 250 MB of information (the data size would become terabytes for a human brain). The resolution of 20 μm is approaching the slice thickness of a thick histology preparation. Although each slice (500×500 pixels in this example) contains much less information compared to a slice of histology, it is not a common practice to make
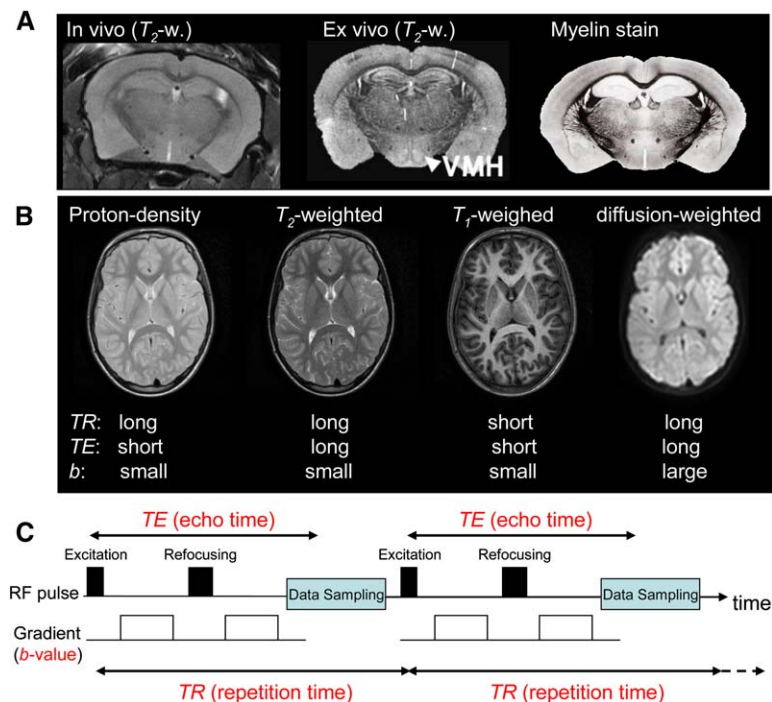
*Correspondence: susumu@mri.jhu.edu

Figure 1. Comparison of Various Types of MRI Contrasts

Examples show mouse MRI (A), human MRI (B), and a diagram of MRI pulse sequence (spin-echo sequence) for definition of acquisition parameters (C). For the mouse images, an in vivo T_2-weighted image (90 μm in-plane resolution and 300 μm slice thickness) and an ex vivo T_2-weighted image (43 μm isotropic resolution) are compared with a myelin-stained histology section. The ex vivo image is provided courtesy of Dr. G. Allan Johnson, Center for In Vivo Microscopy, Duke University, Durham, NC. The myelin-stained section was obtained from the High Resolution Mouse Brain Atlas, available at www.hms.harvard.edu/research/brain/intro.html. For the human images, four different image contrasts are compared. The TE (echo time) and TR (repetition time) are related to the timing of the radio-frequency (RF) pulse and b values are related to a pair of pulsed field gradients. By changing these parameters, the contribution (contrast) of proton density (PD), T_1, T_2, and diffusion weighting can be controlled.

500 serial histology sections. That means that the total amount of data we obtain from one brain with MRI may be equivalent to or surpass the size of the data we obtain histologically. In addition, a comprehensive inspection of 250 MB of anatomical information is often beyond our ability. Therefore, data size, data analysis capacity, and/or our effort could be the real rate-limiting steps in practical situations. These points further underline that image resolution is not always MRI's most severe limitation.

While the images shown in Figure 1A provide an excellent amount of anatomical information, they also reveal a limitation of conventional MRI, which is contrast. As mentioned above, MRI detects signals from protons of water molecules, and it can provide only grayscale images, in which each pixel contains one integer value. Unless two anatomical regions A and B contain water molecules with different physical or chemical properties, these two regions cannot be distinguished from each other with MRI. Otherwise, no matter how high the image resolution is, region A is indistinguishable from region B.

To generate MR contrast based on the physical properties of water molecules, proton density (PD), T_1 and T_2 relaxation times, and the diffusion coefficient (D) are widely used (Figure 1B). The proton density represents water concentration. T_1 and T_2 are signal relaxation (decay) times after excitation, which are related to environmental factors, such as viscosity and the existence of nearby macromolecules. The diffusion term, D, represents the thermal (or Brownian) motion of water molecules. In Equation 1, a simplified equation for the contribution of these parameters to MR signal (S) in a so-called spin-echo image is shown:

$$S = PD(1 - e^{-TR/T_1})e^{-TE/T_2}e^{-bD} \qquad (1)$$

where TR and TE are related to the timing of excitation (called repetition time) and the preparation period (called echo time) of the MR signal, respectively, and b is the diffusion-weighting factor, which will be explained later (Figure 1C). In this equation, the important points are (1) the magnitude of signal from water (S) is the information we obtain from MR scanners; (2) TR, TE, and b are imaging parameters that we can control, and by changing these parameters we can change the contribution (weighting) of T_1, T_2, and D terms to the signal; and (3) MR signal almost always contains a contribution from all four properties of water molecules. Four different types of contrasts generated by spin-echo imaging with different TR, TE, and b factors are demonstrated in Figure 1B.

With only a limited contrast mechanism (PD, T_1, T_2, D) available, it has been a challenging task to interpret contrast changes in MRI and make any conclusions about underlying biological events. To further extend the ability of MRI, we often add another dimension to conventional MRI by acquiring multiple MR images with different imaging parameters, which is sometimes called "quantitative MRI." For example, we can acquire a series of MR images (i.e., multiple signal intensity, S) with different TR or TE to quantify T_1 or T_2, respectively. In this review, we are interested in a new MR imaging modality called diffusion tensor imaging. In this case, we are interested in the diffusion property of a water molecule (D), which can be investigated by performing a series of experiments with different b terms in Equation 1. In the next section, we will try to explain how this technique works in more detail.

What Is Diffusion and Why Is It Important?
The diffusion term, D, represents translational motion of water molecules. This is random thermal motion, also called Brownian motion. Diffusion tensor imaging of live and fixed brains provides similar results (Sun et al., 2005). This reveals three important facts: (1) water molecules move, even in postmortem brains, unless the
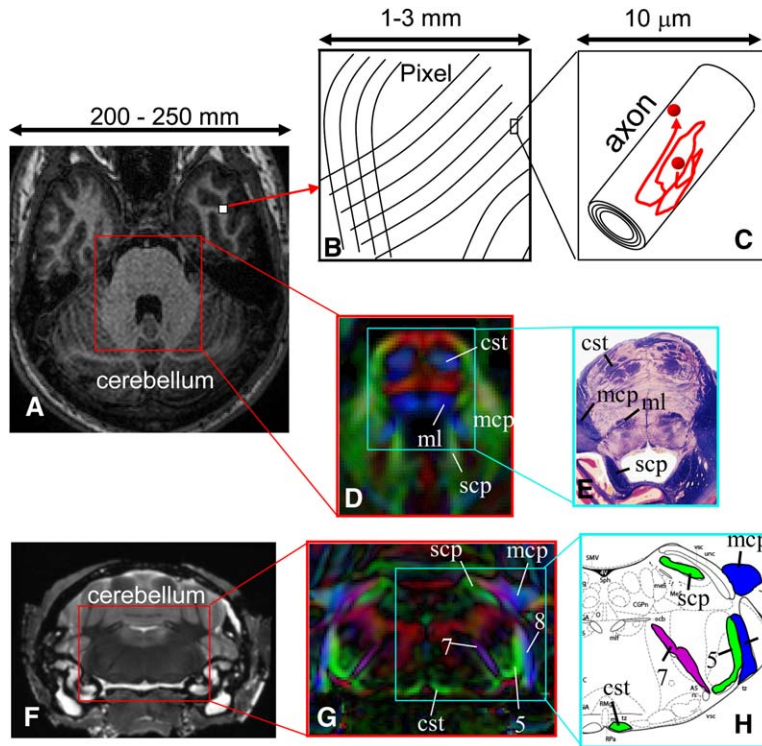
Figure 2. Comparison of Conventional MRI and DTI

Images are from conventional MRI (A and F), DTI (D and G), and histology (E and H). In (B) and (C), spatial relationships between pixels, axonal anatomy, and water diffusion are shown. Image (A) is a T_1-weighted image of the in vivo human brainstem (the pons). Although the white matter looks rather homogeneous in this image, it consists of axonal bundles with complicated architectures (B). The size of the pixels is typically 1–3 mm in clinical DTI, which contains multiple bundles of axons, myelin sheaths, astrocytes, and extracellular spaces (C). The diameters of individual axons are approximately 1–5 μm. During typical diffusion measurement time, water molecules in the brain move approximately 5–10 μm. Because water molecules (red sphere in [C]) see fewer obstacles along the fiber path, the diffusion becomes anisotropic. Image (D) shows a color-coded orientation map created from DTI data (2.5 mm pixel size). In this image, the principal colors (red, green, and blue) represent fibers running along the right-left, anterior-posterior, and superior-inferior orientations. Fibers with an oblique angle have a color that is a mixture of the principal colors. Images (F) and (G) are a T_2-weighted and a color-coded orientation map of a fixed mouse brainstem (120 μm pixel size). cst, corticospinal tract; mcp, middle cerebellar peduncle; ml, medial lemniscus; scp, superior cerebellar peduncle; 5, fifth nerve; 7, seventh nerve; and 8, eighth nerve. The image in (E) is reproduced from *The Human Brain: An Introduction to Its Functional Anatomy* (Nolte, 1998). The image in (H) is from *The Mouse Brain in Stereotaxic Coordinates* (Paxinos and Franklin, 2003) with permissions.

sample is frozen; (2) DTI uses this water motion as a probe to infer the neuroanatomy; and (3) the information DTI carries is dominated by static anatomy and is less influenced by physiology. A useful analogy is the shape of ink dropped on a piece of paper. After the ink is dropped, it begins to spread as the time lapses (strictly speaking, the paper needs to be soaked by water before the ink is applied to avoid capillary action). The spreading of the ink is due to the thermal motion of its molecules, and the shape of the ink stain reveals something about the underlying fiber structure of the paper. When the shape of the ink stain is circular, it is called *isotropic* diffusion. If the stain is elongated along the one axis but not others, this is called *anisotropic diffusion*, suggesting a higher density of fibers oriented in this direction. In DTI, we use this anisotropy to estimate the axonal organization of the brain. Namely, water should move more easily along the axonal bundles rather than perpendicular to these bundles because there are fewer obstacles to prevent movement along the fibers (Figure 2C) (Stejskal, 1965). When we characterize anisotropic diffusion, it provides us with an entirely new image contrast, which is based on structural orientation (Chenevert et al., 1990; Moseley et al., 1990; Turner et al., 1990).

In Figure 2, images created from DTI measurements are compared with conventional MR images. The images show the brainstem of a human (Figure 2D, in vivo data) and a mouse (Figure 2G, ex vivo data). In conventional MRI (Figures 2A and 2F), the brainstem looks rather homogeneous, both in the human and the mouse

study. The color images in Figures 2D and 2G are created from DTI data, in which various colors represent the orientation of aligned structures (mostly axonal orientations), as will be explained in detail later. Using this new contrast, we can now visualize the anatomy of various white matter tracts. This type of axonal delineation could be performed only by postmortem histology (Figures 2E and 2H) in the past.

How Is Diffusion Measured by MRI?

Recalling Equation 1, we already know that the information we obtain from MRI is based on signal intensity, S. Apparently, it is impossible to extract information about diffusion orientation from a single intensity value. If we obtain two images with a different b while other imaging parameters (TR and TE) remain the same, we can retrieve information about the diffusion coefficient, D, from the following equations (Stejskal and Tanner, 1965):

$$\text{Experiment } 1 : S_1 = PD\left(1 - e^{-TR/T_1}\right)e^{-TE/T_2}e^{-b_1 D}$$
$$= S_0 e^{-b_1 D}$$
$$\text{Experiment } 2 : S_2 = S_0 e^{-b_2 D}$$
$$\frac{S_2}{S_1} = e^{-(b_2 - b_1)D} \tag{2}$$
$$D = -\ln\left(\frac{S_2}{S_1}\right)\Big/(b_2 - b_1)$$

In this example, we performed two experiments with different b values (b_1 and b_2) and recorded two different signal intensities (S_1 and S_2). The diffusion coefficient, D, can be calculated from the signal intensity differences between these two studies. Note that terms related to PD, TR, and TE are simplified as S_0
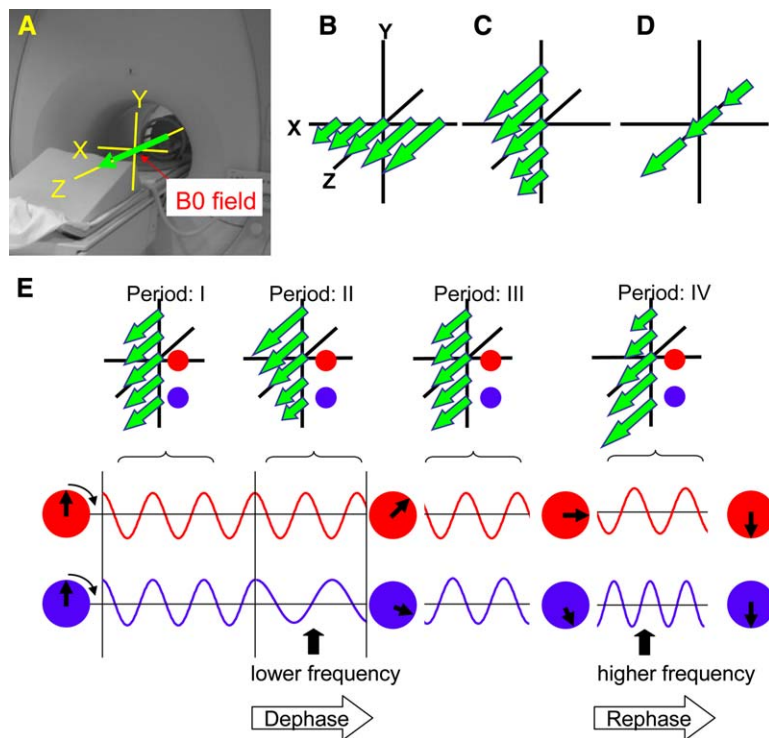
Figure 3. Magnetic Field Gradients and Their Effects on the MRI Signal

The schematic diagrams show the B_0 magnetic field (A), the X, Y, and Z magnetic field gradients (B–D), and the effect on MR signals (E). Orientations and lengths of the green arrows indicate the orientations and strengths of the main magnetic field (B_0). When the gradient is applied, the strength of the B_0 field changes linearly along the gradient axis (B–D). Notice that the gradient of the B_0 field is exaggerated in (B)–(D) for visualization purpose. The actual gradient is less than 5% of the strength of the B_0 field. In (E), Y gradients are applied at time periods II and IV. The durations of the period II and IV are the same, but the orientations of the gradient are opposite. Water signals from two different locations are shown by red and blue colors. The signal frequency is proportional to the strength of the magnetic field B_0.

because they can be treated as constant terms in this example.

To understand the *b* term, we first have to understand magnetic field gradient pulses (simply "gradient" hereafter) (Figure 3). MRI has a strong magnetic field aligned along the bore, called the B_0 field (Figure 3A). For standard clinical MRI scanners, the strength of the magnet is 1.5 Tesla. When a gradient pulse is introduced, the strength of the B_0 field is linearly altered (Figures 3B–3D). MRI scanners are equipped with X, Y, and Z gradient units, and by combining these units, a magnetic field gradient can be introduced along any arbitrary orientation. The frequency of MR signal (ω) and the magnet strength (B_0) have a very simple relationship: $\omega = \gamma B_0$. In Figure 3E, the effect of a gradient pulse is explained using a schematic diagram. Suppose the Y gradient is applied, and signals from water molecules in two different positions along the Y axis are measured (locations shown by red and blue circles). In time period I, all water molecules see the homogeneous B_0 field and thus give the same signal frequency. In time period II, the Y gradient is applied, and water molecules in the blue position begin to resonate at a lower frequency. After the gradient pulse ends (time period III), the signals from the water molecules begin to have the same frequency, but their phases are not the same anymore. In this way, a short period of a gradient pulse introduces a phase difference, depending on the location of the molecules along the gradient axis. Interestingly, we can unwind this phase difference by applying another Y gradient with the opposite polarity (time period IV). In this period, water molecules in the blue location start to resonate at a higher frequency. If the time periods III and IV are the same, we expect perfect refocusing of the phase.

In the diffusion measurement, we use this phase difference to detect water motion (Figure 4). When the first gradient pulse is finished, a gradient of signal phase has been introduced across the sample. The second gradient pulse for the phase refocusing (rewinding of the phase) is applied, typically 20–50 ms after the first pulse. This refocusing is perfect only when the water molecules do not move between the two pulses. If there is translational motion (diffusion) of water molecules, perfect refocusing would fail. Because the signal at each pixel represents the sum of the signals from all the water molecules in that pixel, the imperfect refocusing leads to signal loss. In this way, by applying a pair of gradient pulses, we can sensitize the MR signal to the water diffusion process. Let's look again at Equation 1. As this equation shows, the higher the diffusion coefficient, D, the more signal loss we expect. This is understandable from Figure 4. The term *b* is related to the gradient application. The most intuitive way to change *b* is to lengthen the separation of the two gradient pulses. The longer the separation is, the more time there is for water to move around, which would lead to more signal loss. The exact derivation of the *b* value is beyond the scope of this review, and readers are encouraged to read more advanced review articles (e.g., see Basser and Jones, 2002). The important point is that we can control the amount of the *b* values by changing the strength and timings of the gradient pulses, and, depending on the *b* value, we can expect a different amount of signal loss.

As explained in Equation 2, we need two measurements with different *b* values to determine a diffusion coefficient (Figure 5A). In the first experiment (experiment #1 of Equation 2), a negligible amount of gradient ($b_1 \approx 0$) is applied, and the resultant image is insensitive to the diffusion process (non-diffusion-weighted image, S_1). In the second experiment (experiment #2 of Equation 2, S_2), gradients are applied, and a diffusion-weighted image is obtained. Because of water motion,
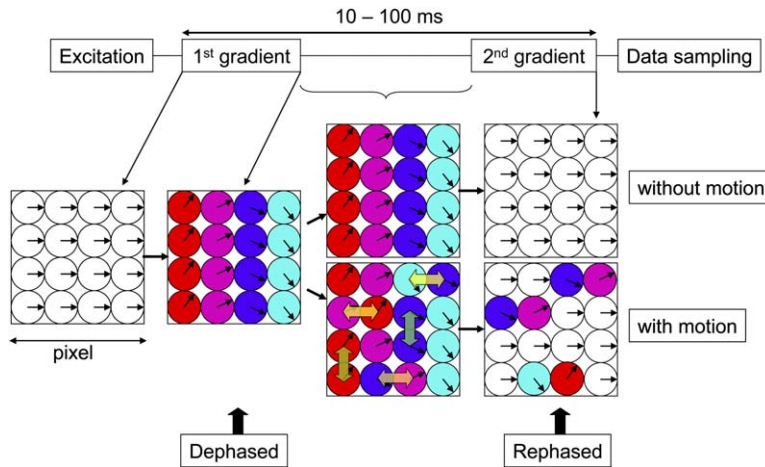
Figure 4. A Schematic Diagram to Explain the Relationship between Water Motion and Gradient Applications

Each circle represents water molecules at different locations within a pixel. The vectors in the circles indicate phases of the signal at each location. If water molecules move in between the two gradient applications, the second gradient cannot perfectly refocus the phases, which leads to signal loss. Note that in this example, horizontal motion (indicated by yellow arrow) leads to the signal loss, but vertical motion (green arrow) does not affect the signal intensity.

this diffusion-weighted image has a lower signal intensity. By solving Equation 2 at each pixel, we can calculate a map of the diffusion coefficient. This is a so-called apparent diffusion coefficient (ADC) map, in which the intensity of each pixel is proportional to the extent of diffusion; water molecules in bright regions diffuse faster than those in dark regions. For example, water in the tissue under the arrowhead has an ADC of 0.49×10^{-3} mm^2/s, and the cerebrospinal fluid has a much higher ADC (3.19×10^{-3} mm^2/s). The reason we use "apparent" is because what we measure may not be a "real" diffusion coefficient. The ADC of water in parenchyma is much slower than that of the cerebrospinal fluid.

This could be partly due to the more viscous environment (low diffusion coefficient) but also due to many obstacles or barriers they encounter during diffusion, such as organelles, protein filaments, and membranes. Namely, the "apparent" reduction of diffusion coefficient may result due to these barriers. When the barriers are aligned along one orientation, the apparent diffusion constants are not the same, depending on the measurement orientation; measurements along the structures lead to higher ADC (less barriers) while measurements perpendicular to it lead to smaller ADC (more barriers). The system thus seems to have anisotropic diffusion, as will be discussed in the next section.

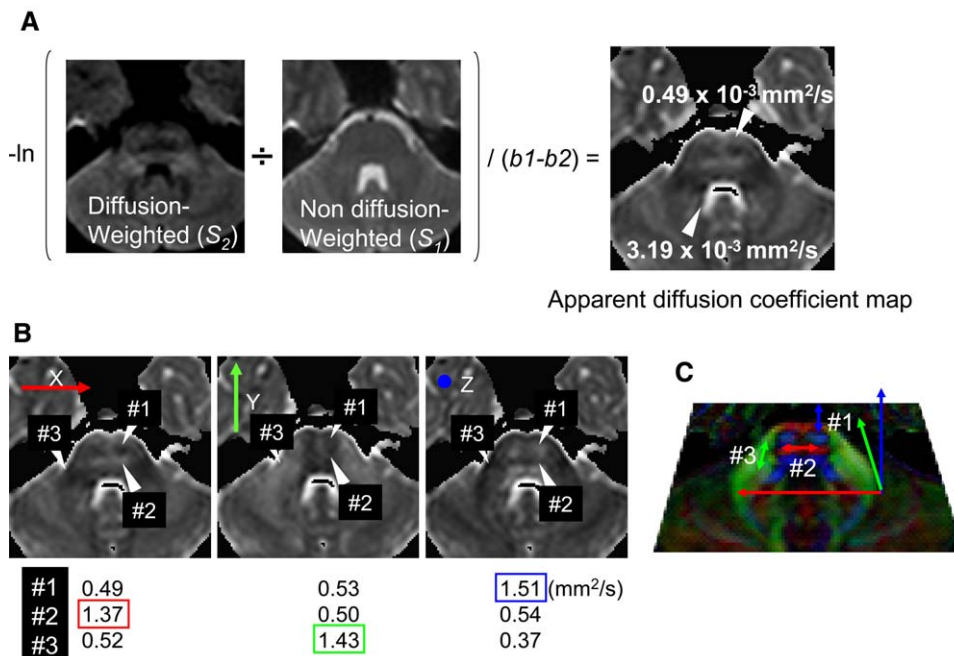|			
#1	0.49	0.53	1.51 (mm²/s)
#2	1.37	0.50	0.54
#3	0.52	1.43	0.37

Figure 5. Apparent Diffusion Constant Maps and Orientation Effects

Apparent diffusion coefficient (ADC) maps are calculated based on Equation 2 (A) and results using the X, Y, and Z axes are compared (B). Two separate scans with different b values ($b_1 \approx 0$ and $b_2 \neq 0$) generate non-diffusion-weighted and diffusion-weighted images in (A). The amount of signal intensity decay (S_1 versus S_2) contains diffusion information, which can be calculated on a pixel-by-pixel basis using Equation 2. In (B), ADCs at three different locations, #1, #2, and #3, are tabulated. From these results, we can identify which measurement orientation yields the highest ADC; Z, X, and Y for location #1, #2, and #3, respectively (indicated by colored boxes). By assigning red, green, and blue for the X, Y, and Z axes, we can display information about the axis with the largest ADC at each pixel (C).
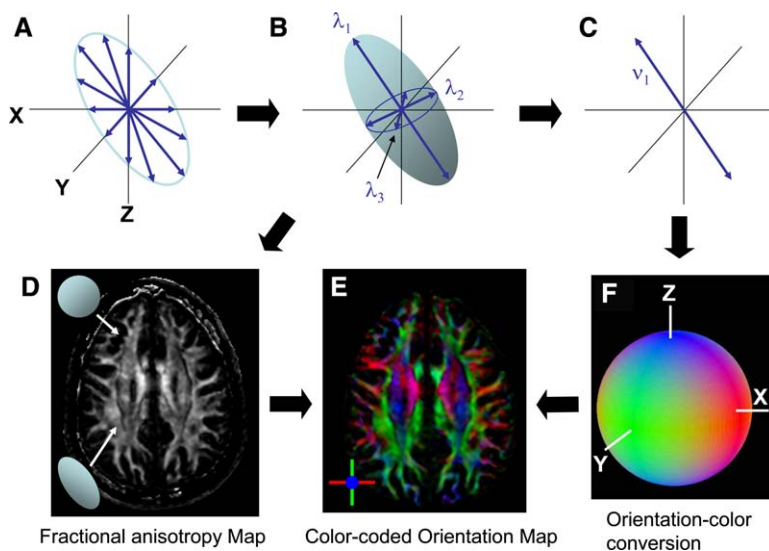
Figure 6. The Principle of DTI and Contrast Generation

From diffusion measurements along multiple axes (A), the shape and the orientation of a "diffusion ellipsoid" is estimated (B). This ellipsoid represents what an ink stain would be if ink were dropped within the pixel. An anisotropy map (D) can be created from the shape, in which dark regions are isotropic (spherical) and bright regions are anisotropic (elongated). From the estimated ellipsoid (B), the orientation of the longest axis can be found (C), which is assumed to represent the local fiber orientation. This orientation information is converted to a color (F) at each pixel. By combining the intensity of the anisotropy map (D) and color (F), a color-coded orientation map is created (E).

MRI Measures Water Diffusion along One Predetermined Axis

One of the most unique features of diffusion measurement by MRI is that it detects water motion only along the applied gradient axis. In Figure 4, the gradient was applied to the horizontal orientation, leading to signal phase dispersion along the horizontal axis. In this case, the translational motion along the horizontal (X) axis (indicated by yellow arrows) leads to signal loss, but the motion along the vertical (Y) axis (indicated by green arrows) has no effect. In this case, we are measuring the ADC along the X axis. By combining the X, Y, and Z gradients, the ADC along any orientation can be measured. In Figure 5B, measurement results along three different orientations (along X, Y, and Z axes) are used. The contrasts of these ADC maps are markedly different, depending on the gradient orientations, which is indicative of anisotropic diffusion. The measured ADCs in three different regions are tabulated under Figure 5B. There is as much as a 3-fold difference in the ADCs, depending on measurement orientations. If water molecules move along axonal fibers, the fiber orientation should be similar to the measurement orientation with the largest ADC (indicated by color boxes). By assigning red, blue, and green colors to the X, Y, and Z axes and by determining the orientation (color) of the largest ADC, we can assign a color for each pixel, thereby creating a color-coded orientation map (Figure 5C). For example, region #1 is assigned a blue color because the ADC is the largest along the Z axis. Similarly, #2 and #3 regions are assigned red and green colors.

Tensor Calculation Is Required to Determine Precise Fiber Orientation

In Figure 5C, fiber orientations are estimated from three independent diffusion measurements along the X, Y, and Z axes. However, these measurements are not enough because fiber orientation is not always along one of the three axes. In reality, fiber orientations are almost always oblique to the axes. To accurately find the orientation with the largest ADC, we would have to measure diffusion along thousands of axes, which is not practical. To simplify this issue, the concept of diffusion tensor was introduced in the early 1990s (Basser et al.,

1994). In this model, measurements along different axes are fitted to a 3D ellipsoid (Figure 6A) (note: the ellipsoid represents average diffusion distance in each direction, not ADC; plotting of ADC along each axis would provide a peanut shape). The properties of the 3D ellipsoid, namely, the length of the longest, middle, and shortest axes (called eigenvalues, λ_1, λ_2, and λ_3) and their orientations (called eigenvectors, v_1, v_2, and v_3) can be defined by six parameters (Figure 6B). Therefore, ADC measurements along six axes are enough to calculate the ellipsoid. To convert the measurement results (more than six ADC) to these six parameters, a 3×3 symmetric matrix called tensor is used, hence the name "diffusion tensor imaging." Once these six parameters are obtained at each pixel, several interesting contrasts can be generated. For example, we can measure the degree of diffusion anisotropy by using a measurement of difference among the three eigenvalues: $(\lambda_1 - \lambda_2)^2 + (\lambda_1 - \lambda_3)^2 + (\lambda_2 - \lambda_3)^2$. If diffusion is isotropic ($\lambda_1 = \lambda_2 = \lambda_3$), this measure becomes 0. Large numbers indicate high diffusion anisotropy. One of the most widely used metrics of diffusion anisotropy is "fractional anisotropy (FA)," which is (Pierpaoli and Basser, 1996):

$$FA = \sqrt{\frac{1}{2}} \frac{\sqrt{\left((\lambda_1 - \lambda_2)^2 + (\lambda_2 - \lambda_3)^2 + (\lambda_3 - \lambda_1)^2\right)}}{\sqrt{\lambda_1^2 + \lambda_2^2 + \lambda_3^2}} \quad (3)$$

This is a very convenient index because it is scaled from 0 (isotropic) to 1 (anisotropic) (Figure 6D).

After a diffusion ellipsoid is determined, the information can be reduced to a vector of the longest axis (eigenvector v_1), which we assume indicates the fiber orientation (Figure 6C). Because it is very difficult to visualize 3D vectors, we usually convert this information to a color space (Figure 6F) and generate a color-coded orientation map (Figure 6E) (Makris et al., 1997; Pajevic and Pierpaoli, 1999).

Three-Dimensional Structures of Axonal Bundles Can Be Reconstructed from DTI Data

If we can assume that the orientation of the longest axis (v_1) of the diffusion tensor represents local fiber orientation, it is not difficult to reconstruct 3D streamlined
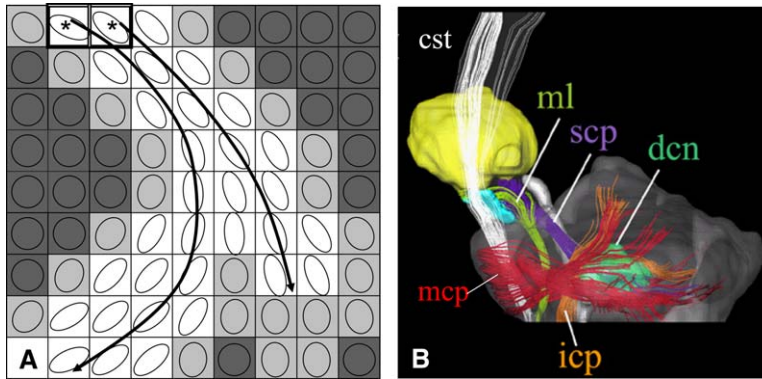
Figure 7. Three-Dimensional Tract Reconstruction

A schematic diagram shows a basic algorithm for tract reconstruction (A) and actual reconstruction results of major white matter tracts in the human brainstem (B). Average fiber orientation is estimated from diffusion anisotropy at each pixel, and a line is propagated from a pixel of interest (pixels with asterisks) following the fiber orientation, until it reaches a brain region of low anisotropy (dark pixels in [A]). cst, corticospinal tract; dcn, dentate nucleus; icp, inferior cerebellar peduncle; mcp, middle cerebellar peduncle; ml, medial lemniscus; and scp, superior cerebellar peduncle.

information from the tensor field (Figure 7A). This method, called tractography, usually requires seeds (pixels with asterisks), from which streamlines are propagated, based on v_1 orientations (Basser et al., 2000; Conturo et al., 1999; Jones et al., 1999; Lazar et al., 2003; Mori et al., 1999; Parker et al., 2002; Poupon et al., 2000). The streamlines are terminated when they reach a low anisotropy region where there is no coherent fiber organization. An example of the 3D reconstruction result of the human brainstem is shown in Figure 7B. In this figure, five major white matter tracts are reconstructed and assigned arbitrary colors for visualization. Comparison of these DTI-based tract reconstructions and postmortem histology-based illustration has shown that tractography can reconstruct core regions of prominent tracts accurately (Catani et al., 2002; Stieltjes et al., 2001). However, this technique is also sensitive to various sources of artifacts, and care must be taken. The limitations of DTI will be discussed later in this review, but for details of the tractography technique, readers are advised to refer to technical reviews (Mori and Van Zijl, 2002).

Practical Aspects of Data Acquisition

In Figure 8, color-coded maps from four different studies are compared. In MRI, scanning time, image resolution, and signal-to-noise ratio (SNR) are all related. For example, to reduce noise, we need to increase signal averaging (scanning time) or reduce image resolution. One of the shortcomings of DTI is that it is inherently a low-

SNR and slow imaging technique. For example, in vivo human DTI usually has a pixel resolution of 2–3 mm with 5–15 min of scanning time with the employment of state-of-the art rapid imaging technologies, such as multislice 2D imaging, echo-planar imaging (EPI), and parallel imaging. For in vivo studies, there is another reason why we use EPI, which can capture an image within 100–150 ms. DTI, which is sensitive to small molecular motions, is prone to various types of artifacts caused by physiological motion. DTI of human brain, for example, was made possible only after this type of rapid imaging was introduced (Turner et al., 1990). The rapid imaging techniques, on the other hand, have several drawbacks. EPI suffers from image distortion and limited spatial resolution. The distortion becomes more severe in higher magnetic fields, and it is not a practical choice for small animal studies performed on high-field magnets (>4.7 T). The multislice 2D imaging is time efficient, and a 3D volume can be reconstructed by stacking the 2D slices. However, the slice thickness (Z axis resolution) cannot be thinner than a certain limit: approximately 1 mm (human scanners) or 0.2 mm (animal scanners). As a result, the long scanning time is often a limiting factor in performing DTI in small animals. The images and imaging parameters in Figure 8 should provide an idea about what kind of image resolution we can expect within a reasonable imaging time, which, in turn, suggests which white matter structures we can investigate.
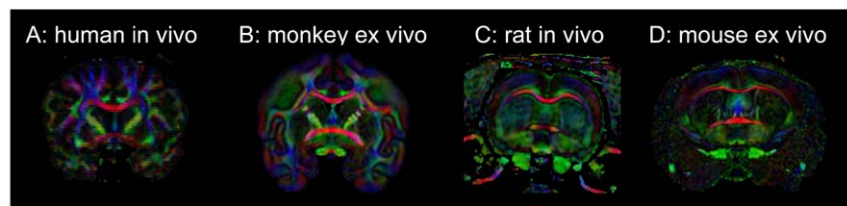
	A: human in vivo	B: monkey ex vivo	C: rat in vivo	D: mouse ex vivo
Magnet:	1.5 T	4.7T	9.4T	11.7T
Data size:	96x96x60	186x256x192	96x80x64	400x200x160
Pixel size (mm):	2.5x2.5x2.5	0.31x0.31x0.31	0.30x0.30x1.0	0.13x0.13x0.13
Imaging time:	12 min	30 hours	1.5 hours	24 hours
Image type:	multi-slice EPI-SE	3D SE	multi-slice SE	3D SE

Figure 8. Examples of Brain DTI of Different Animals and Imaging Parameters

Images are (A) in vivo human, (B) ex vivo macaque monkey, (C) in vivo rat, and (D) ex vivo mouse brains. For rodent imaging, scanning time under sedation can only last up to 2–3 hr. Lengthy true 3D imaging is, thus, not suitable, and we need to resort to more time-efficient multislice 2D imaging, in which the resolution of the Z axis is practically limited to 0.2–0.5 mm. For ex vivo studies, in which scanning time is not a limiting factor, we can use 3D imaging, in which resolution can be as high as the scanning time and SNR allow. EPI indicates echo-planar imaging, and SE indicates spin-echo imaging.

For example, it would be difficult to study a white matter tract with 1 mm diameter for in vivo human studies but would be quite feasible for ex vivo mouse studies.

Advantages and Limitations of DTI

DTI provides two types of new contrasts: diffusion anisotropy and fiber orientation (Figure 6), which carries rich anatomical information about the white matter. Although the white matter looks homogeneous on conventional MRI, it, in fact, has a very complex structure. DTI contrasts are sensitive to such complexity. However, interpretation of the results is not always straightforward. As discussed in the Introduction, MRI picks up signal from protons of water molecules. When attempting to connect MRI observation to the underlying neuroanatomy, there is always a certain amount of ambiguity. It is important to understand which anatomical information can be retrieved with high confidence and which cannot. Below are several examples of the limitations associated with this technique.

Issue of Anterograde and Retrograde Orientation. In DTI, we are observing the motion of water molecules, from which we cannot differentiate the directionality of axons.

Issue of Macroscopic and Microscopic Anatomical Factors. In Figures 2A–2C, relative dimensions of the image pixels (typically 2–3 mm) and the diffusion process (1–10 μm during the 20–100 ms of diffusion application period) are illustrated. When diffusion is anisotropic, water molecules encounter many aligned obstacles within the range of 1–10 μm of the translational motion. In the white matter, some of these obstacles include protein filaments, cell membrane, and myelin, all of which have strongly aligned structures (Beaulieu, 2002). Diffusion anisotropy thus carries microscopic (cellular level) anatomical information (Figure 2C). However, the microscopic information is averaged over the large voxel volume. If there are multiple fiber populations with different fiber orientations, their contributions to the signal could be averaged. As a matter of fact, the cortex has low anisotropy (FA < 0.2), not because there are no fibers, but because axon and dendrite orientations are not normally aligned within the large voxels in human cortex. If we can improve image resolution, we are likely to see higher anisotropy in the cortex. We observe diffusion anisotropy only when there are microscopic sources of diffusion anisotropy AND there is macroscopic homogeneity of the structures within a pixel (Figure 2B). If we find changes in diffusion anisotropy, we cannot immediately conclude that the source of abnormalities lies in cellular level structures, such as myelin and axons; it could be due to the reorganization of axons at macroscopic levels.

Issue of Simplification by Tensor Calculation. The issue of macroscopic factors is closely related to the tensor calculation. In Figure 6, the process of the tensor calculation is explained. After ADC measurements along multiple axes (Figure 6A), the results are fitted to a six-parameter elliptic shape (Figure 6B). At this point, there could be a large amount of information reduction, because the calculation assumes that fiber structures are homogeneous within a pixel, and, therefore, we can neglect the macroscopic anatomic factors. The assumption that the largest diffusion axis corresponds to the fiber orientation is not true if there are two fiber populations; one orientation cannot represent the orientations of two fiber populations. There are two ways to reduce this problem and extract more anatomical information. First, we can increase image resolution. The amount of information in each pixel does not change, but we have fewer populations of tracts within a pixel and the total amount of pixels (and anatomical information) within the brain increases. Second, we can abandon the six-parameter tensor approach and extract more parameters from each pixel. Currently, many alternatives to the simple tensor approach are being proposed (Frank, 2001; Tournier et al., 2004; Tuch et al., 2003; Wedeen et al., 2005).

Sensitivity to Motion and Scanning Time. DTI detects the motion of water, which is about 5–10 μm during the measurement time. Any physiological motions of this magnitude could interfere with DTI, making the result inaccurate. The relatively long scanning time required for DTI also has adverse effects on the suppression of physiological motions. Later in this review, imaging of mouse fetuses is introduced. This type of DTI requires an image resolution of less than 100 μm, and the imaging time approaches 24 hr. In vivo fetal DTI would be, thus, extremely difficult. The throughput of ex vivo DTI could be, on the other hand, improved in the future due to improvements in microimaging hardware, employment of relaxation-enhancement agents, such as gadolinium, and, more recently, new techniques to scan multiple samples at a time (Bock et al., 2003; Johnson et al., 2002).

Application Studies of DTI

A simple literature search using "diffusion," "tensor," and "imaging" results in more than 300 publications in 2005 alone, and it is beyond the scope of this review to comprehensively cover the DTI studies. In this section, we would like to focus on several state-of-the-art application studies that will help to deepen the understanding of DTI and its potentials for basic neuroscience research (for extensive review of DTI applications, readers are advised to refer to a review by Horsfield and Jones, 2002).

Measurement of Anisotropy as a Marker of Pathological States

It has been shown that relaxation-based parameters such as T_1, T_2, and magnetization transfer are heavily influenced by myelin concentration, making them markers of myelin status. High-diffusion anisotropy, on the other hand, could be observed in unmyelinated nerves, indicating that the axon is an important factor for the anisotropy (Beaulieu and Allen, 1994). Figure 9 shows images from an ex vivo rat spinal cord sample with possible white matter lesions caused by injections of lysolecithin (Hall, 1972). Both conventional MRI and DTI were able to identify a lesion in the dorsal column white matter (Figures 9A and 9B). The MRI results suggested that both myelin and axonal loss were present in the sample. The location information was used to guide subsequent histological analysis, which agreed with the MRI results (Figures 9C and 9D). Because the images in Figure 9 were obtained from a fixed tissue, one may wonder about the usefulness of the MRI data, because the sample can be examined by histology. In this study, the role of MRI is very similar to gross
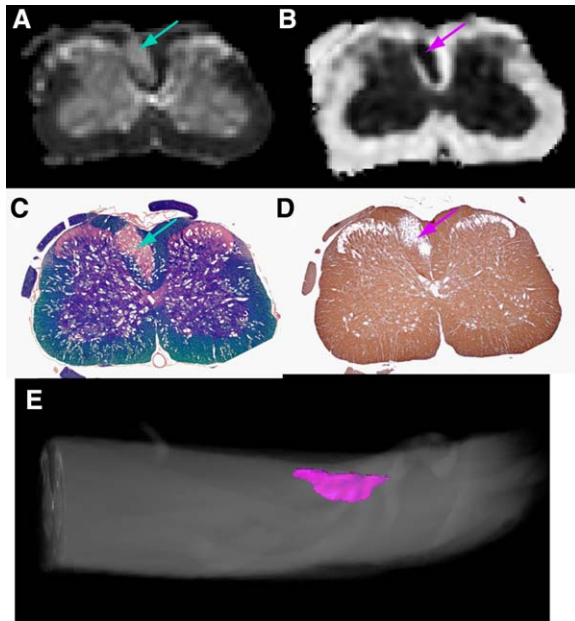
Figure 9. Application of DTI to Study Lysolecithin-Induced White Matter Lesions in a Rat Spinal Cord

In axial T_2-weighted and FA map images ([A] and [B], respectively), the blue and purple arrows indicate the white matter lesion. Matching histological sections with Luxol Fast Blue (C) and SMI-31 (D) staining reveals loss of myelin and phosphorylated neurofilament in the lesion, respectively. The lesion location was reconstructed three-dimensionally based on the FA map and shown in (E). The images are courtesy of Dr. Peter Calabresi, Johns Hopkins University.

necropsies prior to histopathology, which can effectively direct subsequent histology studies to affected regions. In this case, these lesions are not visible from the outside, and without MRI we would choose locations for histology somewhat blindly. Another important role for MRI/DTI is that once the histology-MRI/DTI correlation

is established, we can examine the extent of lesions three-dimensionally, as shown in Figure 9E.

Although the resolution is lower than in ex vivo studies, in vivo rodent DTI is also becoming feasible due to recent advancements in hardware and imaging techniques (see e.g., Figure 8C). This allows us to monitor longitudinal changes in anisotropy of the same animal. For example, in recent works by Sun et al., demyelination process by cuprizone administration was monitored by in vivo DTI (Sun et al., 2006). Loss of anisotropy was evident in the white matter after the administration and subsequent histology studies confirmed good correlation with myelin loss.

Note that there are three possibilities that would lead to lower anisotropy: an increase in transverse (short axes) diffusivity (called type 1 anisotropy loss hereafter), a decrease in axial (the longest axis) diffusivity (type 2 anisotropy loss), and the combination of the two (type 3 anisotropy loss). Demyelination and axonal injury both result in lower anisotropy, but animal studies have shown evidence that demyelination often leads to type 1 loss, and axonal injury leads to type 2 anisotropy loss (Song et al., 2002). One of the explanations for these results is that demyelination causes less restriction (diffusion barrier) in transverse diffusivity and that axonal injury causes a disarray of axons that reduces axial diffusivity.

Anisotropy Change during Brain Development

DTI studies of developing brains also provide important information about diffusion anisotropy. In Figures 10A–10C, T_2 and anisotropy maps of mouse brains are compared at three different developmental stages. As shown in Figure 1, the contrast of a T_2-weighted image of an adult mouse brain is dominated by myelination. In the embryonic and neonatal period, when myelination has not begun, the brain has a long T_2, and, as myelination progresses, T_2 shortens considerably (Figure 10D). The initial rapid decrease in T_2 occurs in the first 3 weeks
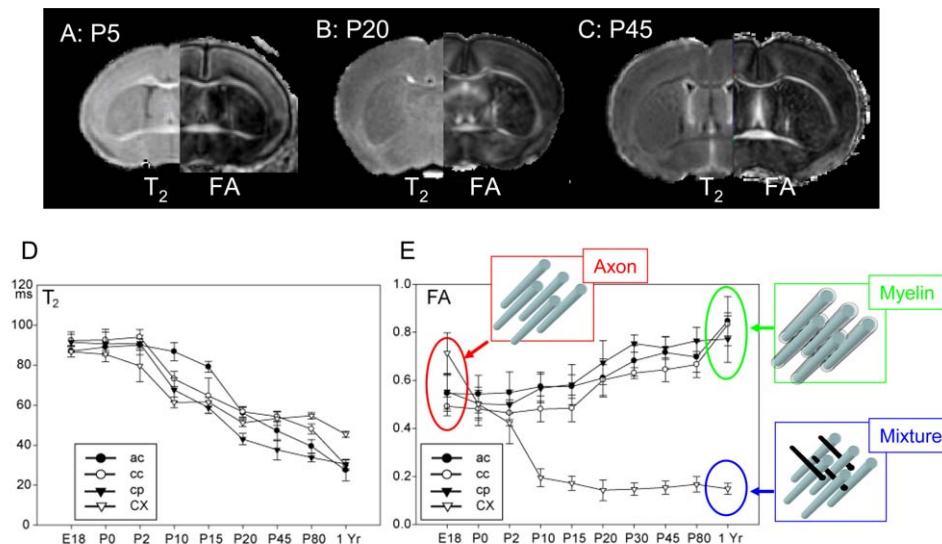

Figure 10. Typical Time Courses of T_2 and Anisotropy of the Brain during Development

Images in (A)–(C) show T_2 (left) and FA (right) map of neonate brains at P5, P20, and P45. Graphs in (D) and (E) show time courses of T_2 and FA of selected brain regions. ac, anterior commissure; cc, corpus callosum; cp, cerebral peduncle; and CX, cortex.
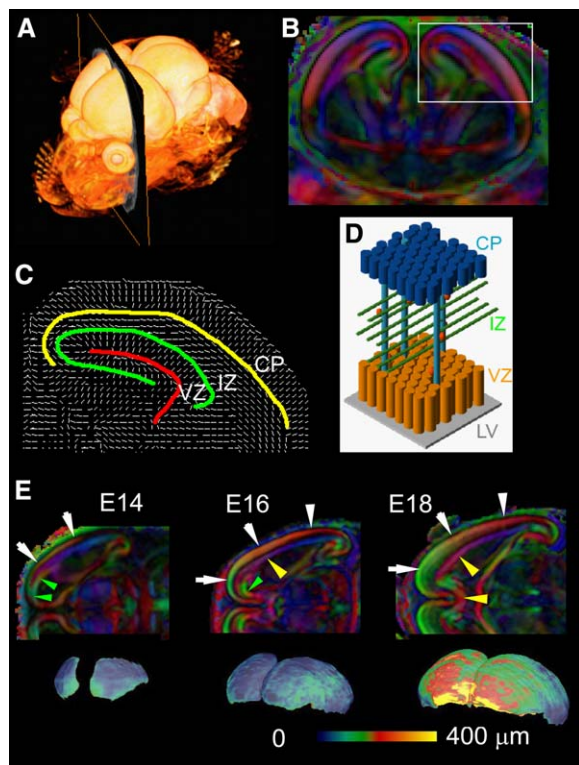
Figure 11. DTI of Developing Mouse Embryos

Images show DTI of an E16 mouse embryo brain (A–D) and cortical development during E14–E18 period (E). The 3D volume rendering (A) shows the location of a coronal slice used for (B) and (C). (B) is a color-coded orientation map at the level of the anterior commissure. (C) is a vector map showing orientations of fiber architectures. The red line indicates the location of the ventricle, the green line the boundary between the ventricle zone (VZ) and the intermediate zone (IZ), and the yellow line the boundary between the IZ and the cortical plate (CP). (D) is a schematic diagram of the fiber structures of the VZ, IZ, and CP. Neurons (red spheres) are born in the VZ surrounding the lateral ventricle (LV) and migrate to the CP along radial glia (blue vertical lines). Between the VZ and CP layers, axons (green horizontal lines) start to grow, forming the IZ. The fiber angles delineated in (C) agree with the known cortical architectures in (D). In (E), the emerging CPs are indicated by white arrows in color-coded orientation maps. Below the maps, three-dimensional views of manually defined CPs and their thickness measurement results are shown. Yellow and green arrows indicate locations of the IZ and the VZ. Note that the CP and the IZ continue to grow during development while the VZ diminishes.

in the mouse, which agrees very well with that of myelination period, further supporting the idea that T_2 contrast is dominated by myelination.

The typical time courses for anisotropies of the gray and white matter are shown in Figure 10E. Several important facts can be derived from this data set. First, relatively high anisotropy (0.3–0.5) can be found in the premyelinated cortex and white matter structures. This clearly indicates that myelination is not required for diffusion anisotropy. After birth, the anisotropy of the white matter further increases. This is likely due to myelination of the axons, although it could also be due to an increase in axonal density or axon caliber. Interestingly, anisotropy of the cortex decreases rapidly in the first 2 weeks after birth in mouse brains (Mori et al., 2001; Zhang et al.,

2003). The high anisotropy of the cortex in neonates, followed by a rapid decrease, has also been observed in human and cat brains and is attributed to dendrite growth, which destroys the coherent water motion along the columnar organization of the axons in the cortex (Baratti et al., 1999; Mukherjee et al., 2002; Neil et al., 1998, 2002; Thornton et al., 1997). These data exemplify how microscopic factors (e.g., axons and myelin) and macroscopic fiber architectures (a mixture of fibers with different orientations) can affect diffusion anisotropy. They also clearly illustrate that myelination is not a required factor for anisotropy (Beaulieu and Allen, 1994), but, possibly, an augmenting factor.

Anatomy Studies of Premyelinated Brains

The data about developing brains also illustrate the importance of fiber orientation contrast obtained from DTI. In premyelinated brains, conventional T_1- and T_2-weighted images provide poor contrast by which to study the brain anatomy. Anisotropy and orientation-based contrast (color maps), on the other hand, carry rich anatomical information about premature brains (Baratti et al., 1999; Huppi et al., 1998; Mukherjee et al., 2002; Neil et al., 1998). Figure 11 shows images of developing mouse embryos (Zhang et al., 2003). At E16, a three-layer structure of the cortex can be clearly appreciated, which includes the ventricular zone, the intermediate zone, and the cortical plate (Figures 11B and 11C). The vector map (Figure 11C) shows radiating fiber orientations in the neuroepithelium and cortical plate, in concordance with the existence of radial glia (Figure 11D) and invading axons in the intermediate zone, which run tangential to the brain surface (Rakic, 1972). For these structures that are visualized and characterized by MRI-histology comparison, we now have a tool to examine their anatomical status three-dimensionally in the entire brain from one data set. In Figure 11E, color-coded orientation maps of developing brains are shown at 48 hr intervals from E14 to E18. The development of the cortical plate (white arrows) and white matter tracts (yellow arrowheads), as well as shrinkage of the ventricular zone (green arrowheads), are clearly depicted. These visualized structures are easily delineated three-dimensionally. As an example, the cortical plates are manually defined, and their thicknesses are mapped at the surfaces (Figure 11F). The cortical plates emerge from the lateral regions of the hemispheres from E13–E14, growing toward the midline, and by E16 the cortical plates cover the entire hemisphere. After the completion of the coverage, the cortical plates thicken, especially in the medio-frontal cortex. This type of 3D quantification is extremely difficult to perform with histology. Using the 3D reconstruction technology shown in Figure 7, trajectories of developing white matter tracts can also be visualized to investigate axonal growth (Zhang et al., 2003).

With the currently achievable imaging resolution (up to 60 μm) and within a practical imaging time (up to 24 hr), DTI is suitable for studying embryos as young as E11–E12. Samples from earlier stages are small enough to study with a limited number of histology slices or with whole-mount scanning electron microscopy. In addition, the increased transparency of the embryo samples allows us to use optical imaging, further diminishing the advantage of MRI/DTI for the investigation of embryos in earlier stages.

Phenotype Characterization by High-Resolution DTI

Phenotype characterization is one of the promising application fields for this relatively new imaging technique (Bock et al., 2003; Johnson et al., 2002; MacKenzie-Graham et al., 2004; Nieman et al., 2006; Wang et al., 2006; Zhang et al., 2005). Compared to histology, MRI/DTI excels in two different types of anatomical characterization. One is the efficient prehistology screening of the entire brain, and the other is the quantification of anatomical shapes and sizes. Light and electron microscopy can examine samples at a limited number of locations where histology slices are prepared. Therefore, histology-based methods are often hypothesis driven so that we can extract slices at optimum locations and angles. There is always the possibility that important phenotypes are overlooked with this approach. In addition, it is often important to study the time evolution of phenotypes to understand the role of a gene of interest. Specifically, we need to know when and how the phenotype begins during development. For example, if we have a phenotype of abnormally thin cortex or missing white matter tracts, it is important to know whether the phenotype is due to abnormal formation of the structures or to degeneration of once normally formed structures. This requires a description of the vast 4D anatomical domain. Rapid screening by a 3D imaging method would, thus, greatly enhance the efficiency of our study.

White Matter Parcellation and Connectivity Studies

As can be seen in Figure 2, orientation information can reveal locations of white matter bundles that cannot be identified by conventional MRI. In other words, DTI has a potential to parcellate the white matter into smaller anatomical units. If the boundaries of such units are sharply defined, a structure of interest can be manually defined (similar to Figure 2H). We can also consider the tractography (Figure 7) as a type of the parcellation tools, with which pixels that belong to the same white matter tract are grouped together. These parcellation tools allow us to monitor status (such as volume, T_1, T_2, FA, and ADC) of the white matter in a tract-specific manner (for example, see a comprehensive paper by Pagani et al., 2005). Tractography is also used to investigate brain connectivity. For example, cortex-white matter connectivity (Catani et al., 2002; Lazar and Alexander, 2005; Stieltjes et al., 2001) and cortico-thalamic connectivity (Behrens et al., 2003) have been investigated and indicated excellent correlation with histology-based knowledge. In the future, these approaches may become an important modality to investigate association between the gray and white matter and its abnormalities.

Conclusion

We have seen how diffusion tensor imaging works and have explored several potential uses for this technique. DTI is now becoming widely available in clinical scanners and human clinical studies are actively being performed. On the other hand, high-resolution DTI technology and applications to animal studies for basic neuroscience research have started only recently. In vivo DTI allows us to monitor the longitudinal evolution of axonal injuries and the efficacy of interventions in various disease models. We can correlate the findings with his-tology to investigate disease mechanisms. Ex vivo DTI provides far greater image resolution, and the orientation-based contrast is a powerful tool for the characterization of brain development and abnormalities (phenotypes). Because of the recent advent of ever more sophisticated imaging technology, high-quality DTI results are becoming more and more available and the throughput is improving substantially. Future advancements in this technology will, no doubt, provide even more potential applications in this exciting research field.

References

Ahrens, E.T., Laidlaw, D.H., Readhead, C., Brosnan, C.F., Fraser, S.E., and Jacobs, R.E. (1998). MR microscopy of transgenic mice that spontaneously acquire experimental allergic encephalomyelitis. Magn. Reson. Med. 40, 119–132.

Baratti, C., Barnett, A., and Pierpaoli, C. (1999). Comparative MR imaging study of brain maturation in kittens with t1, t2, and the trace of the diffusion tensor. Radiology 210, 133–142.

Basser, P.J., and Jones, D.K. (2002). Diffusion-tensor MRI: theory, experimental design and data analysis - a technical review. NMR Biomed. 15, 456–467.

Basser, P.J., Mattiello, J., and Le Bihan, D. (1994). MR diffusion tensor spectroscopy and imaging. Biophys. J. 66, 259–267.

Basser, P.J., Pajevic, S., Pierpaoli, C., Duda, J., and Aldroubi, A. (2000). In vitro fiber tractography using DT-MRI data. Magn. Reson. Med. 44, 625–632.

Beaulieu, C. (2002). The basis of anisotropic water diffusion in the nervous system - a technical review. NMR Biomed. 15, 435–455.

Beaulieu, C., and Allen, P.S. (1994). Determinants of anisotropic water diffusion in nerves. Magn. Reson. Med. 31, 394–400.

Behrens, T.E., Johansen-Berg, H., Woolrich, M.W., Smith, S.M., Wheeler-Kingshott, C.A., Boulby, P.A., Barker, G.J., Sillery, E.L., Sheehan, K., Ciccarelli, O., et al. (2003). Non-invasive mapping of connections between human thalamus and cortex using diffusion imaging. Nat. Neurosci. 6, 750–757.

Bock, N.A., Konyer, N.B., and Henkelman, R.M. (2003). Multiple-mouse MRI. Magn. Reson. Med. 49, 158–167.

Catani, M., Howard, R.J., Pajevic, S., and Jones, D.K. (2002). Virtual in vivo interactive dissection of white matter fasciculi in the human brain. Neuroimage 17, 77–94.

Chenevert, T.L., Brunberg, J.A., and Pipe, J.G. (1990). Anisotropic diffusion in human white matter: Demonstration with MR technique in vivo. Radiology 177, 401–405.

Conturo, T.E., Lori, N.F., Cull, T.S., Akbudak, E., Snyder, A.Z., Shimony, J.S., McKinstry, R.C., Burton, H., and Raichle, M.E. (1999). Tracking neuronal fiber pathways in the living human brain. Proc. Natl. Acad. Sci. USA 96, 10422–10427.

Frank, L.R. (2001). Anisotropy in high angular resolution diffusion-weighted MRI. Magn. Reson. Med. 45, 935–939.

Hall, S.M. (1972). The effect of injections of lysophosphatidyl choline into white matter of the adult mouse spinal cord. J. Cell Sci. 10, 535–546.

Harsan, L.A., Poulet, P., Guignard, B., Steibel, J., Parizel, N., de Sousa, P.L., Boehm, N., Grucker, D., and Ghandour, M.S. (2006). Brain dysmyelination and recovery assessment by noninvasive

in vivo diffusion tensor magnetic resonance imaging. J. Neurosci. Res. *83*, 392–402.

Horsfield, M.A., and Jones, D.K. (2002). Applications of diffusion-weighed and diffusion tensor MRI to white matter diseases. NMR Biomed. *15*, 570–577.

Huppi, P., Maier, S., Peled, S., Zientara, G., Barnes, P., Jolesz, F., and Volpe, J. (1998). Microstructural development of human newborn cerebral white matter assessed in vivo by diffusion tensor magnetic resonance imaging. Pediatr. Res. *44*, 584–590.

Jacobs, R.E., and Fraser, S.E. (1994). Imaging neuronal development with magnetic resonance imaging (NMR) microscopy. J. Neurosci. Methods *54*, 189–196.

Johnson, G.A., Benveniste, H., Black, R.D., Hedlund, L.W., Maronpot, R.R., and Smith, B.R. (1993). Histology by magnetic resonance microscopy. Magn. Reson. Q. *9*, 1–30.

Johnson, G.A., Cofer, G.P., Fubara, B., Gewalt, S.L., Hedlund, L.W., and Maronpot, R.R. (2002). Magnetic resonance histology for morphologic phenotyping. J. Magn. Reson. Imaging *16*, 423–429.

Jones, D.K., Simmons, A., Williams, S.C., and Horsfield, M.A. (1999). Non-invasive assessment of axonal fiber connectivity in the human brain via diffusion tensor MRI. Magn. Reson. Med. *42*, 37–41.

Kroenke, C.D., Bretthorst, G.L., Inder, T.E., and Neil, J.J. (2006). Modeling water diffusion anisotropy within fixed newborn primate brain using Bayesian probability theory. Magn. Reson. Med. *55*, 187–197.

Lazar, M., and Alexander, A.L. (2005). Bootstrap white matter tractography (BOOT-TRAC). Neuroimage *24*, 524–532.

Lazar, M., Weinstein, D.M., Tsuruda, J.S., Hasan, K.M., Arfanakis, K., Meyerand, M.E., Badie, B., Rowley, H.A., Haughton, V., Field, A., and Alexander, A.L. (2003). White matter tractography using diffusion tensor deflection. Hum. Brain Mapp. *18*, 306–321.

MacKenzie-Graham, A., Lee, E.F., Dinov, I.D., Bota, M., Shattuck, D.W., Ruffins, S., Yuan, H., Konstantinidis, F., Pitiot, A., Ding, Y., et al. (2004). A multimodal, multidimensional atlas of the C57BL/6J mouse brain. J. Anat. *204*, 93–102.

Makris, N., Worth, A.J., Sorensen, A.G., Papadimitriou, G.M., Reese, T.G., Wedeen, V.J., Davis, T.L., Stakes, J.W., Caviness, V.S., Kaplan, E., et al. (1997). Morphometry of in vivo human white matter association pathways with diffusion weighted magnetic resonance imaging. Ann. Neurol. *42*, 951–962.

Mori, S., and Van Zijl, P.C. (2002). Fiber tracking: principles and strategies - a technical review. NMR Biomed. *15*, 468–480.

Mori, S., Crain, B.J., Chacko, V.P., and van Zijl, P.C.M. (1999). Three dimensional tracking of axonal projections in the brain by magnetic resonance imaging. Ann. Neurol. *45*, 265–269.

Mori, S., Itoh, R., Zhang, J., Kaufmann, W.E., van Zijl, P.C.M., Solaiyappan, M., and Yarowsky, P. (2001). Diffusion tensor imaging of the developing mouse brain. Magn. Reson. Med. *46*, 18–23.

Moseley, M.E., Cohen, Y., Kucharczyk, J., Mintorovitch, J., Asgari, H.S., Wendland, M.F., Tsuruda, J., and Norman, D. (1990). Diffusion-weighted MR imaging of anisotropic water diffusion in cat central nervous system. Radiology *176*, 439–445.

Mukherjee, P., Miller, J.H., Shimony, J.S., Philip, J.V., Nehra, D., Snyder, A.Z., Conturo, T.E., Neil, J.J., and McKinstry, R.C. (2002). Diffusion-tensor MR imaging of gray and white matter development during normal human brain maturation. AJNR Am. J. Neuroradiol. *23*, 1445–1456.

Nair, G., Tanahashi, Y., Low, H.P., Billings-Gagliardi, S., Schwartz, W.J., and Duong, T.Q. (2005). Myelination and long diffusion times alter diffusion-tensor-imaging contrast in myelin-deficient shiverer mice. Neuroimage *28*, 165–174.

Neil, J., Shiran, S., McKinstry, R., Schefft, G., Snyder, A., Almli, C., Akbudak, E., Arnovitz, J., Miller, J., Lee, B., and Conturo, T. (1998). Normal brain in human newborns: apparent diffusion coefficient and diffusion anisotropy measured by using diffusion tensor MR imaging. Radiology *209*, 57–66.

Neil, J., Miller, J., Mukherjee, P., and Huppi, P.S. (2002). Diffusion tensor imaging of normal and injured developing human brain - a technical review. NMR Biomed. *15*, 543–552.

Nieman, B.J., Flenniken, A.M., Adamson, S.L., Henkelman, R.M., and Sled, J.G. (2006). Anatomical phenotyping in the brain and skull of a mutant mouse by magnetic resonance imaging and computed tomography. Physiol. Genomics *24*, 154–162.

Nolte, J. (1998). The Human Brain: An Introduction to Its Functional Anatomy, Fourth Edition (St. Louis: C.V. Mosby).

Pagani, E., Filippi, M., Rocca, M.A., and Horsfield, M.A. (2005). A method for obtaining tract-specific diffusion tensor MRI measurements in the presence of disease: application to patients with clinically isolated syndromes suggestive of multiple sclerosis. Neuroimage *26*, 258–265.

Pajevic, S., and Pierpaoli, C. (1999). Color schemes to represent the orientation of anisotropic tissues from diffusion tensor data: application to white matter fiber tract mapping in the human brain. Magn. Reson. Med. *42*, 526–540.

Parker, G.J., Stephan, K.E., Barker, G.J., Rowe, J.B., MacManus, D.G., Wheeler-Kingshott, C.A., Ciccarelli, O., Passingham, R.E., Spinks, R.L., Lemon, R.N., and Turner, R. (2002). Initial demonstration of in vivo tracing of axonal projections in the macaque brain and comparison with the human brain using diffusion tensor imaging and fast marching tractography. Neuroimage *15*, 797–809.

Paxinos, G., and Franklin, K.B.J. (2003). The Mouse Brain in Stereotaxic Coordinates, Second Edition (San Diego, CA: Academic Press).

Pierpaoli, C., and Basser, P.J. (1996). Toward a quantitative assessment of diffusion anisotropy. Magn. Reson. Med. *36*, 893–906.

Poupon, C., Clark, C.A., Frouin, V., Regis, J., Bloch, L., Le Bihan, D., and Mangin, J.F. (2000). Regularization of diffusion-based direction maps for the tracking of brain white matter fascicules. Neuroimage *12*, 184–195.

Rakic, P. (1972). Mode of cell migration to the superficial layers of fetal monkey neocortex. J. Comp. Neurol. *145*, 61–83.

Smith, B.R., Linney, E., Huff, D.S., and Johnson, G.A. (1996). Magnetic resonance microscopy of embryos. Comput. Med. Imaging Graph. *20*, 483–490.

Song, S.K., Sun, S.W., Ramsbottom, M.J., Chang, C., Russell, J., and Cross, A.H. (2002). Dysmyelination revealed through MRI as increased radial (but unchanged axial) diffusion of water. Neuroimage *17*, 1429–1436.

Stejskal, E. (1965). Use of spin echoes in a pulsed magnetic-field gradient to study restricted diffusion and flow. J. Chem. Phys. *43*, 3597–3603.

Stejskal, E.O., and Tanner, J.E. (1965). Spin diffusion measurement: spin echoes in the presence of a time-dependent field gradient. J. Chem. Phys. *42*, 288.

Stieltjes, B., Kaufmann, W.E., van Zijl, P.C.M., Fredericksen, K., Pearlson, G.D., and Mori, S. (2001). Diffusion tensor imaging and axonal tracking in the human brainstem. Neuroimage *14*, 723–735.

Sun, S.W., Neil, J.J., Liang, H.F., He, Y.Y., Schmidt, R.E., Hsu, C.Y., and Song, S.K. (2005). Formalin fixation alters water diffusion coefficient magnitude but not anisotropy in infarcted brain. Magn. Reson. Med. *53*, 1447–1451.

Sun, S.W., Liang, H.F., Trinkaus, K., Cross, A.H., Armstrong, R.C., and Song, S.K. (2006). Noninvasive detection of cuprizone induced axonal damage and demyelination in the mouse corpus callosum. Magn. Reson. Med. *55*, 302–308.

Thornton, J.S., Ordidge, R.J., Penrice, J., Cady, E.B., Amess, P.N., Punwani, S., Clemence, M., and Wyatt, J.S. (1997). Anisotropic water diffusion in white and gray matter of the neonatal piglet brain before and after transient hypoxia-ischaemia. Magn. Reson. Imaging *15*, 433–440.

Tournier, J.D., Calamante, F., Gadian, D.G., and Connelly, A. (2004). Direct estimation of the fiber orientation density function from diffusion-weighted MRI data using spherical deconvolution. Neuroimage *23*, 1176–1185.

Tuch, D.S., Reese, T.G., Wiegell, M.R., and Wedeen, V.J. (2003). Diffusion MRI of complex neural architecture. Neuron *40*, 885–895.

Turner, R., Le Bihan, D., Maier, J., Vavrek, R., Hedges, L.K., and Pekar, J. (1990). Echo-planar imaging of intravoxel incoherent motion. Radiology *177*, 407–414.

Wang, Y., Zhang, J., Mori, S., and Nathans, J. (2006). Axonal growth and guidance defects in Frizzled3 knock-out mice: a comparison of diffusion tensor magnetic resonance imaging, neurofilament staining, and genetically directed cell labeling. J. Neurosci. *26*, 355–364.

Wedeen, V.J., Hagmann, P., Tseng, W.Y., Reese, T.G., and Weisskoff, R.M. (2005). Mapping complex tissue architecture with diffusion spectrum magnetic resonance imaging. Magn. Reson. Med. *54*, 1377–1386.

Zhang, J., Richards, L.J., Yarowsky, P., Huang, H., van Zijl, P.C., and Mori, S. (2003). Three-dimensional anatomical characterization of the developing mouse brain by diffusion tensor microimaging. Neuroimage *20*, 1639–1648.

Zhang, J., Chen, Y.B., Hardwick, J.M., Miller, M.I., Plachez, C., Richards, L.J., Yarowsky, P., van Zijl, P., and Mori, S. (2005). Magnetic resonance diffusion tensor microimaging reveals a role for Bcl-x in brain development and homeostasis. J. Neurosci. *25*, 1881–1888.